

## Partitioned coupling strategies for fluid-structure interaction with large displacement: Explicit, implicit and semi-implicit schemes

Tao He<sup>\*1,2</sup>

<sup>1</sup>Department of Civil Engineering, Shanghai Normal University, Shanghai 201418, China

<sup>2</sup>School of Civil Engineering, University of Birmingham, Birmingham B15 2TT, UK

(Received August 26, 2014, Revised January 15, 2015, Accepted January 21, 2015)

**Abstract.** In this paper the unsteady fluid-structure interaction (FSI) problems with large structural displacement are solved by partitioned solution approaches in the arbitrary Lagrangian-Eulerian finite element framework. The incompressible Navier-Stokes equations are solved by the characteristic-based split (CBS) scheme. Both a rigid body and a geometrically nonlinear solid are considered as the structural models. The latter is solved by Newton-Raphson procedure. The equation governing the structural motion is advanced by Newmark- $\beta$  method in time. The dynamic mesh is updated by using moving submesh approach that cooperates with the ortho-semi-torsional spring analogy method. A mass source term (MST) is introduced into the CBS scheme to satisfy geometric conservation law. Three partitioned coupling strategies are developed to take FSI into account, involving the explicit, implicit and semi-implicit schemes. The semi-implicit scheme is a mixture of the explicit and implicit coupling schemes due to the fluid projection splitting. In this scheme MST is renewed for interfacial elements. Fixed-point algorithm with Aitken's  $\Delta^2$  method is carried out to couple different solvers within the implicit and semi-implicit schemes. Flow-induced vibrations of a bridge deck and a flexible cantilever behind an obstacle are analyzed to test the performance of the proposed methods. The overall numerical results agree well with the existing data, demonstrating the validity and applicability of the present approaches.

**Keywords:** fluid-structure interaction; arbitrary Lagrangian-Eulerian; finite element method; coupling scheme; vortex-induced vibrations; large displacement

### 1. Introduction

Fluid-structure interaction (FSI) characterizes the interplay between a fluid and a structure via an interface which separates the fluid and structural domains. Possessing great practical interest, FSI is a frequent event in a wide variety of engineering realms. For instance, the natural wind over a high-rise building or a suspension bridge (Choi and Yu 2000, Morgenthal and McRobie 2002) and liquid sloshing in a container (Eswaran *et al.* 2013, Keivani and Shooshtari 2013, Nagashima and Tsukuda 2013, Keivani *et al.* 2014) are typical FSI phenomena in civil engineering. As a consequence, FSI is a significant consideration both for the design and computation of an engineering structure. Because of the sophisticated coupling effect existing between two completely different media, FSI poses one of the most challenging topics in computational fluid

---

\*Corresponding author, Ph.D., E-mail: [txh317@bham.ac.uk](mailto:txh317@bham.ac.uk)

dynamics (CFD).

Typically, partitioned coupling approach is the preferred strategy to tackle the numerical solution of FSI. The partitioned approach strategically solves different disciplines in a sequential manner, facilitating the marriage of the existing programs with minimal changes and allowing for a flexible choice of various efficient solvers. These traits make the partitioned approach a very appealing solution technique in practice. The partitioned coupling approaches can be further classified as the explicit scheme (Wall and Ramm 1998, He *et al.* 2012) and the implicit scheme (He *et al.* 2014, He 2015a, b). From the computational viewpoint, the explicit scheme is efficient since it works in a subiteration-free fashion. However, the explicit scheme does not assure the exact satisfaction of the equilibrium on the fluid-structure interface so that the accumulative errors may produce a spurious solution or even a failure. Under certain circumstances, e.g. haemodynamics, the explicit scheme suffers from the severely numerical instability initiated by the inherent time lag effect. By comparison, the implicit scheme preserves the energy balance exactly and holds the numerical stability well by performing subiterations per time step although it is time consuming. Obviously, the implicit scheme is physically rigorous. A great number of endeavors have been devoted to design various implicit schemes, e.g., (Matthies and Steindorf 2003, Dettmer and Perić 2006a, Dettmer and Perić 2006b, Küttler and Wall 2008, Yamada and Yoshimura 2008, He *et al.* 2014, He 2015b, He 2015a).

A third category of the partitioned approaches is the semi-implicit scheme which has been recently proposed by Fernández *et al.* (Fernández *et al.* 2007) to face the strong added-mass effect (Causin *et al.* 2005, Förster *et al.* 2007). In (Fernández *et al.* 2007) the concept of the semi-implicit or partial-implicit coupling depends on the Chorin-Témam splitting (Chorin 1968, Témam 1968) where the ALE-advection-diffusion step (explicit coupling substep) is explicitly treated with a predicted mesh movement while the projection step (implicit coupling substep) on the known fluid mesh is implicitly coupled with the structural motion. The theoretical analysis in (Fernández *et al.* 2007) indicated that the main strength of this scheme originates from its enhanced computational efficiency without affecting the stability condition too much, compared to the implicit scheme. Breuer *et al.* (Breuer and Münsch 2008a, Breuer and Münsch 2008b, Breuer *et al.* 2012) independently devised a semi-implicit scheme called the partitioned semi-implicit predictor-corrector coupling scheme, which was implemented by connecting code packages both for fluid and structure. Following the basic framework of (Fernández *et al.* 2007), Murea (Murea 2007) presented a semi-implicit strategy using the augmented Lagrangian method to preserve the interfacial consistency of the velocity and stress. For the same purpose, Sy and Murea (Sy and Murea 2008, Murea and Sy 2009) solved a least squares problem on the fluid-structure interface and presented the stability analysis of their algorithm (Sy and Murea 2008). The Broyden-Fletcher-Goldfarb-Shanno iterations were employed to calculate the resultant optimization problem on the frozen fluid mesh. Quaini and Quarteroni (Quaini and Quarteroni 2007) invented a semi-implicit scheme using the algebraic fractional step method. Badia *et al.* (Badia *et al.* 2008) introduced several semi-implicit schemes using the inexact block-LU factorization. Astorino *et al.* proposed a Nitsche-based semi-implicit coupling scheme (Astorino *et al.* 2009b) and a Robin-based semi-implicit coupling scheme (Astorino *et al.* 2009a) for the better stability properties. As a supplement of (Fernández *et al.* 2007), Astorino and Grandmont (Astorino and Grandmont 2010) provided a convergence analysis for the projection-based semi-implicit coupling scheme. They proved that the error estimate in finite time was derived and the error of time discretization in the scheme was proved to be  $\sqrt{\Delta t}$  at least from theoretical and numerical

viewpoints. Recently, He *et al.* (He *et al.* 2014) developed a semi-implicit for flow-induced vibrations of a bluff body based on the hybrid interface conditions.

Fernández (Fernández 2011) firstly presented a review for the numerical simulations of blood flows in large arteries involving the implicit, semi-implicit and explicit coupling schemes. We are motivated to work on the formulation of efficient FSI solvers in terms of different coupling schemes, and this paper aims at presenting a promising application of the CBS scheme on the unsteady FSI problems. The foundation is the reality that the CBS scheme makes use of the classical Chorin-Témam splitting (Chorin 1968, Témam 1968). Therefore, the CBS scheme can serve not only within the fluid subproblem but also within the whole coupling algorithm, as will be shown later. On the other hand, the applications of the CBS scheme on FSI are still tedious. The present work entails an innovative use of the CBS scheme which is quite different from those frequently encountered in the previously published works.

The remainder of this paper is organized as follows. The fluid problem is depicted in Sections 2 while the structural problem is presented in Sections 3. The dynamic mesh technique is introduced in Section 4. Section 5 provides the interface coupling conditions. The partitioned coupling schemes are interpreted in Section 6. Numerical examples are investigated in Section 7 and some conclusions are drawn in the final section.

## 2. Fluid model

### 2.1 Governing equations

We define  $\Omega^F \subset \mathbb{R}^2$  as an open bounded fluid domain with the spatial coordinate  $\mathbf{x}$  and  $[0, T]$  as a temporal domain with the temporal coordinate  $t$ . The fluid boundary  $\Gamma^F$  consists of three nonoverlapping segments, i.e.,  $\Gamma^F = \Gamma_D^F \cup \Gamma_N^F \cup \Sigma$ , where  $\Gamma_D^F$ ,  $\Gamma_N^F$  and  $\Sigma$  respectively denote the Dirichlet, Neumann and interfacial boundaries. The governing equations for an incompressible fluid flow on the moving mesh are the Navier-Stokes (NS) equations written in the arbitrary Lagrangian-Eulerian (ALE) description, stating the conservation laws of mass and momentum as

$$\nabla \cdot \mathbf{u} = 0 \quad \text{in } \Omega^F \times [0, T] \tag{1}$$

$$\rho^F \left( \frac{\partial \mathbf{u}}{\partial t} + \mathbf{c} \cdot \nabla \mathbf{u} - \mathbf{f}^F \right) - \nabla \cdot \boldsymbol{\tau}^F = \mathbf{0} \quad \text{in } \Omega^F \times [0, T] \tag{2}$$

where  $\nabla$  represents the gradient operator,  $\rho^F$  the fluid density,  $\mathbf{u}$  the fluid velocity,  $\mathbf{c} = \mathbf{u} - \mathbf{w}$  the convective velocity,  $\mathbf{w}$  the mesh velocity,  $\mathbf{f}^F$  the fluid body force and  $\boldsymbol{\tau}^F$  the fluid stress tensor.

The constitutive equation for a Newtonian fluid reads as

$$\boldsymbol{\tau}^F = -p\mathbf{I} + 2\mu\boldsymbol{\varepsilon}^F \quad \text{in } \Omega^F \times [0, T] \tag{3}$$

$$\boldsymbol{\varepsilon}^F = \frac{1}{2}(\nabla \mathbf{u} + (\nabla \mathbf{u})^T) \quad \text{in } \Omega^F \times [0, T] \tag{4}$$

where  $p$  denotes the fluid pressure,  $\mathbf{I}$  the identity matrix,  $\mu$  the dynamic viscosity,  $\boldsymbol{\varepsilon}^F$  the rate-of-strain tensor and superscript T transpose. The appropriate initial and boundary conditions are prescribed in order to complete the fluid equations.

Giving the free-stream velocity  $U$  and the reference dimension  $D$ , the following dimensionless variables are defined

$$\mathbf{x}^* = \frac{\mathbf{x}}{D}, \quad t^* = \frac{tU}{D}, \quad \mathbf{u}^* = \frac{\mathbf{u}}{U}, \quad \mathbf{c}^* = \frac{\mathbf{c}}{U}, \quad p^* = \frac{p}{\rho^F U^2}, \quad \mathbf{f}^{F,*} = \frac{\mathbf{f}^F D}{U^2}$$

Introducing the above variables and dropping all asterisks, the dimensionless NS equations are obtained as follows

$$\nabla \cdot \mathbf{u} = 0 \quad \text{in } \Omega^F \times [0, T] \quad (5)$$

$$\frac{\partial \mathbf{u}}{\partial t} + \mathbf{c} \cdot \nabla \mathbf{u} - \nabla \cdot \boldsymbol{\tau}^F - \mathbf{f}^F = \mathbf{0} \quad \text{in } \Omega^F \times [0, T] \quad (6)$$

$$\boldsymbol{\tau}^F = -p\mathbf{I} + \frac{1}{Re} (\nabla \mathbf{u} + (\nabla \mathbf{u})^T) \quad \text{in } \Omega^F \times [0, T] \quad (7)$$

where  $Re = \frac{\rho^F D U}{\mu}$  is the Reynolds number.

## 2.2 Characteristic-based split (CBS) scheme

A general solution technique for CFD has been originally proposed by the trilogy of Zienkiewicz and his co-workers (Zienkiewicz and Codina 1995, Zienkiewicz *et al.* 1995, Codina *et al.* 1998) since 1995, and it was formally named the CBS scheme in 1999 (Zienkiewicz *et al.* 1999). In the present paper the incompressible NS equations are solved by the semi-implicit CBS scheme, whose procedure is carried out by the following steps

*Step 1:* Calculate the intermediate velocity field

$$\tilde{\mathbf{u}} - \mathbf{u}^n = \Delta t \left( -\mathbf{c}^n \cdot \nabla \mathbf{u}^n + \frac{1}{Re} \nabla^2 \mathbf{u}^n + \frac{\Delta t}{2} \mathbf{c}^n \cdot \nabla (\mathbf{c}^n \cdot \nabla \mathbf{u}^n) \right) \quad (8)$$

*Step 2:* Update the pressure field

$$\nabla^2 p^{n+1} = \frac{1}{\Delta t} \nabla \cdot \tilde{\mathbf{u}} \quad (9)$$

*Step 3:* Correct the velocity field

$$\mathbf{u}^{n+1} - \tilde{\mathbf{u}} = -\Delta t \left( \nabla p^{n+1} - \frac{\Delta t}{2} \mathbf{c}^n \cdot \nabla^2 p^n \right) \quad (10)$$

where  $\tilde{\mathbf{u}}$  indicates the intermediate velocity and  $\Delta t$  is the time step. In the above algorithm the body force  $\mathbf{f}^F$  and the third-order term are omitted.

The stability conditions require the time step to satisfy the following criterion (Zienkiewicz and

Codina 1995, Zienkiewicz *et al.* 1995)

$$\Delta t \leq \min(\Delta t_{\text{DIF}}, \Delta t_{\text{CON}}) \quad (11)$$

where  $\Delta t_{\text{DIF}} = \frac{1}{2} Re(\bar{\Delta})^2$  is the local diffusive time step,  $\Delta t_{\text{CON}} = \frac{\bar{\Delta}}{|\mathbf{u}_{\text{CON}}|}$  the local convective time step,  $\bar{\Delta}$  the characteristic element size, and  $\mathbf{u}_{\text{CON}}$  the convective element velocity.

### 2.3 Spatial discretization

The spatial discretization is established by using the standard Galerkin finite element method (FEM). The fluid variables are approximated by

$$\mathbf{u} = \mathbf{N}_u \mathbf{u}_h \quad \text{and} \quad p = \mathbf{N}_p \mathbf{p}_h \quad (12)$$

where  $\mathbf{N}_u$  and  $\mathbf{N}_p$  are the shape functions of the fluid finite elements, and subscript  $h$  means a nodal quantity. The final matrix form of the three steps can be written as

$$\mathbf{M}_u (\tilde{\mathbf{u}}_h - \mathbf{u}_h^n) = \Delta t \left( -\mathbf{Q} \mathbf{u}_h^n + \mathbf{K}_\tau \mathbf{u}_h^n + \frac{\Delta t}{2} \mathbf{K}_u \mathbf{u}_h^n \right) \quad (13)$$

$$\mathbf{H} \mathbf{p}_h^{n+1} = \frac{1}{\Delta t} \mathbf{B} \tilde{\mathbf{u}}_h \quad (14)$$

$$\mathbf{M}_u (\mathbf{u}_h^{n+1} - \tilde{\mathbf{u}}_h) = -\Delta t \left( \mathbf{B}^T \mathbf{p}_h^{n+1} - \frac{\Delta t}{2} \mathbf{P} \mathbf{p}_h^n \right) \quad (15)$$

where the coefficient matrices are defined as

$$\begin{aligned} \mathbf{M}_u &= \int_{\Omega^F} \mathbf{N}_u^T \mathbf{N}_u \, d\Omega, \quad \mathbf{Q} = \int_{\Omega^F} \mathbf{N}_u^T (\nabla(\mathbf{c}^n \mathbf{N}_u)) \, d\Omega, \quad \mathbf{K}_\tau = \frac{1}{Re} \int_{\Omega^F} (\nabla \mathbf{N}_u)^T (\nabla \mathbf{N}_u) \, d\Omega, \\ \mathbf{K}_u &= -\frac{1}{2} \int_{\Omega^F} (\nabla^T(\mathbf{c}^n \mathbf{N}_u))^T (\nabla^T \mathbf{c}^n \mathbf{N}_u) \, d\Omega, \quad \mathbf{H} = \int_{\Omega^F} (\nabla \mathbf{N}_p)^T (\nabla \mathbf{N}_p) \, d\Omega, \\ \mathbf{B} &= \int_{\Omega^F} (\nabla \mathbf{N}_p)^T \mathbf{N}_u \, d\Omega, \quad \mathbf{P} = \int_{\Omega^F} (\nabla \mathbf{c}^n \mathbf{N}_u)^T (\nabla \mathbf{N}_p) \, d\Omega \end{aligned}$$

A linear three-node triangular (T3) element is considered because it is very convenient to use an equal-order and low-order interpolation for the fluid velocity and pressure in the CBS scheme. To reduce the time consumption, the lumped mass matrix is adopted herein.

### 3. Structural model

A rigid or flexible structure immersed in a fluid sustains the fluctuating fluid force and can be modeled as a mass-spring-dashpot system. The structural domain  $\Omega^S \in \mathfrak{R}^2$  is bounded by the boundary  $\Gamma^S$  which includes three complementary subsets  $\Gamma_D^S$ ,  $\Gamma_N^S$  and  $\Sigma$  where  $\Gamma_D^S$  and

$\Gamma_N^S$  are the Dirichlet and Neumann boundaries respectively. The equation governing the structural motion is described from the Lagrangian viewpoint by

$$\mathbf{M} \frac{d^2 \mathbf{d}}{dt^2} + \mathbf{C} \frac{d\mathbf{d}}{dt} + \mathbf{K} \mathbf{d} = \mathbf{F} \quad (16)$$

where  $\mathbf{d}$  is the structural displacement,  $\mathbf{M}$ ,  $\mathbf{C}$  and  $\mathbf{K}$  represent the mass, damping and stiffness matrices of the structure respectively, and  $\mathbf{F}$  is the applied force delivered by the surrounding fluid. The structural velocity and acceleration are formulated as  $\mathbf{v} = \frac{d\mathbf{d}}{dt}$  and

$\mathbf{a} = \frac{d\mathbf{v}}{dt} = \frac{d^2 \mathbf{d}}{dt^2}$ . For simplicity, the initial and boundary conditions are ignored in the structural model. The time marching scheme of Eq. (16) utilizes the famous Newmark- $\beta$  method which is unconditionally stable if  $\beta \geq 0.25$  and  $\gamma \geq 0.5$  (Newmark 1959).

### 3.1 Rigid body case

In the planar case the motion of a rigid body is controlled by three uncoupled displacement components defined at the center of gravity. The structural displacement is defined as  $\mathbf{d}^T = \{d_1 \ d_2 \ \theta\}$  where  $d_1$  is the horizontal component,  $d_2$  the vertical component and  $\theta$  the rotational component. Because  $\mathbf{M}$ ,  $\mathbf{C}$  and  $\mathbf{K}$  are diagonal, Eq. (16) is reduced to

$$\begin{bmatrix} m_1 & & \\ & m_2 & \\ & & m_\theta \end{bmatrix} \frac{d^2 \mathbf{d}}{dt^2} + \begin{bmatrix} c_1 & & \\ & c_2 & \\ & & c_\theta \end{bmatrix} \frac{d\mathbf{d}}{dt} + \begin{bmatrix} k_1 & & \\ & k_2 & \\ & & k_\theta \end{bmatrix} \mathbf{d} = \mathbf{F} \quad (17)$$

where  $m_i$ ,  $c_i$  and  $k_i$  ( $i = 1, 2$  and  $\theta$ ) represent the mass, damping and stiffness of the structure respectively. Note that  $m_\theta$  is the structural mass moment of inertia and the compatibility condition (Nomura and Hughes 1992) must be fulfilled.

The dimensionless variables and the reduced parameters are defined as follows

$$\begin{aligned} \mathbf{x}^* &= \frac{\mathbf{x}}{D}, \quad t^* = \frac{tU}{D}, \quad d_1^* = \frac{d_1}{D}, \quad d_2^* = \frac{d_2}{D}, \\ C_D &= \frac{F_D}{0.5\rho^F D U^2}, \quad C_L = \frac{F_L}{0.5\rho^F D U^2}, \quad C_M = \frac{F_M}{0.5\rho^F D^2 U^2}, \\ \zeta_1 &= \frac{c_1}{2\sqrt{m_1 k_1}}, \quad \zeta_2 = \frac{c_2}{2\sqrt{m_2 k_2}}, \quad \zeta_\theta = \frac{c_\theta}{2\sqrt{m_\theta k_\theta}}, \\ f_{1,R} &= \frac{f_{1,N} D}{U}, \quad f_{2,R} = \frac{f_{2,N} D}{U}, \quad f_{\theta,R} = \frac{f_{\theta,N} D}{U}, \end{aligned}$$

$$f_{1,N} = \frac{1}{2\pi} \sqrt{\frac{k_1}{m_1}}, \quad f_{2,N} = \frac{1}{2\pi} \sqrt{\frac{k_2}{m_2}}, \quad f_{\theta,N} = \frac{1}{2\pi} \sqrt{\frac{k_\theta}{I_\theta}},$$

$$m_1^* = \frac{m_1}{\rho^F D^2}, \quad m_2^* = \frac{m_2}{\rho^F D^2}, \quad m_\theta^* = \frac{m_\theta}{\rho^F D^4}$$

where  $F_D$ ,  $F_L$  and  $F_M$  denote the fluid drag, lift and pitching moment respectively,  $C_D$ ,  $C_L$  and  $C_M$  are the associated fluid coefficients,  $\zeta_i$  ( $i = 1, 2$  and  $\theta$ ) is the damping ratio,  $f_{i,R}$  ( $i = 1, 2$  and  $\theta$ ) is the reduced natural frequency,  $f_{i,N}$  ( $i = 1, 2$  and  $\theta$ ) is the natural frequency, and  $m_i^*$  ( $i = 1, 2$  and  $\theta$ ) is the mass ratio.

After discarding asterisks, Eq. (17) is nondimensionalized as follows

$$\frac{d^2 \mathbf{d}}{dt^2} + 4\pi \begin{bmatrix} f_{1,R} \zeta_1 & & \\ & f_{2,R} \zeta_2 & \\ & & f_{\theta,R} \zeta_\theta \end{bmatrix} \frac{d\mathbf{d}}{dt} + \begin{bmatrix} (2\pi f_{1,R})^2 & & \\ & (2\pi f_{2,R})^2 & \\ & & (2\pi f_{\theta,R})^2 \end{bmatrix} \mathbf{d} = \begin{Bmatrix} \frac{C_D}{2m_1^*} \\ C_L \\ \frac{C_M}{2m_\theta^*} \end{Bmatrix} \quad (18)$$

### 3.2 Elastic body case

The governing equation for the structural motion of an elastic solid interprets the principle of conservation of linear momentum cast in the total Lagrangian formulation by

$$\rho^S \left( \frac{d^2 \mathbf{d}}{dt^2} - \mathbf{f}^S \right) - \nabla \cdot \boldsymbol{\tau}^S = \mathbf{0} \quad \text{in } \Omega^S \times [0, T] \quad (19)$$

where  $\rho^S$  is the structural density,  $\mathbf{f}^S$  the structural body force and  $\boldsymbol{\tau}^S$  the Cauchy stress tensor. The second Piola-Kirchhoff stress tensor  $\mathbf{S}$  which is related to  $\boldsymbol{\tau}^S$  via a geometric transformation is given by

$$\mathbf{S} = J \mathbf{G}^{-1} \boldsymbol{\tau}^S \mathbf{G}^{-T} \quad (20)$$

where  $\mathbf{G} = \mathbf{I} + \nabla \mathbf{d}$  is the deformation gradient tensor and  $J = \det(\mathbf{G})$ .

The Saint Venant-Kirchhoff material model is specified to account for the geometrically nonlinear behavior as follow

$$\mathbf{S} = \mathbf{C} : \mathbf{E} \quad \text{and} \quad \mathbf{E} = \frac{1}{2} (\mathbf{G}^T \mathbf{G} - \mathbf{I}) \quad (21)$$

where  $\mathbf{C}$  stand for the constitutive tensor and  $\mathbf{E}$  Green-Lagrangian strain tensor. In addition, Young's modulus  $E$  and Poisson's ratio  $\nu$  must be prescribed for the flexible structure.

To enable the nondimensionalization of Eq. (19), the following dimensionless variables are

defined

$$\mathbf{x}^* = \frac{\mathbf{x}}{D}, \quad t^* = \frac{tU}{D}, \quad \mathbf{d}^* = \frac{\mathbf{d}}{D}, \quad E^* = \frac{E}{\rho^F U^2}, \quad \mathbf{f}^{S,*} = \frac{\mathbf{f}^S D}{U^2}$$

Similarly, we can build the dimensionless version of the governing Eq. (19) as

$$\frac{d^2 \mathbf{d}}{dt^2} - \frac{1}{m^*} \nabla \cdot \boldsymbol{\tau}^S - \mathbf{f}^S = \mathbf{0} \quad \text{in } \Omega^S \times [0, T] \quad (22)$$

where  $m^* = \frac{\rho^S}{\rho^F}$  is the mass ratio.

### 3.3 Spatial discretization

For the spatial discretization by FEM, the structural variables are approximated as

$$\mathbf{d} = \mathbf{N}_v \mathbf{d}_h, \quad \mathbf{v} = \mathbf{N}_v \mathbf{v}_h \quad \text{and} \quad \mathbf{a} = \mathbf{N}_v \mathbf{a}_h \quad (23)$$

where  $\mathbf{N}_v$  is the shape function of the structural finite element. A quadratic nine-node quadrilateral (Q9) plane stress element is employed for the structural analysis.

The weak form of Eq. (22) can be obtained based on the principle of virtual work. By substituting Eq. (23) into the weak form and ignoring the damping effect, the matrix form of the structural equation is gained at element level below

$$\mathbf{M} \frac{d^2 \mathbf{d}}{dt^2} + \mathbf{K} \mathbf{d} = \mathbf{F} \quad (24)$$

with the following approximations

$$\mathbf{M} = \int_{\Omega^S} \mathbf{N}_v^T \mathbf{N}_v d\Omega, \quad \mathbf{K} = \frac{1}{m^*} \int_{\Omega^S} \mathbf{B}_v^T \mathbf{C} \mathbf{B}_v d\Omega, \quad \mathbf{F} = \int_{\Omega^S} \mathbf{N}_v^T \mathbf{f}^S d\Omega + \int_{\Gamma_N^S} \mathbf{N}_v^T \mathbf{h}^S d\Gamma,$$

$$\boldsymbol{\varepsilon}^S = \mathbf{B}_v \mathbf{d}_h, \quad \mathbf{B}_v = \mathbf{L} \mathbf{N}_v$$

where  $\boldsymbol{\varepsilon}^S$  denotes the structural strain,  $\mathbf{B}_v$  the strain matrix and  $\mathbf{L}$  the differential operator.

In order to perform the dynamic analysis of the geometrically nonlinear structure, the incremental equilibrium form of Eq. (24) is set up by

$$\mathbf{K}_T^n \Delta \mathbf{d} = \mathbf{F}^{n+1} - \mathbf{R}^n - \mathbf{M} \frac{d^2 \mathbf{d}^{n+1}}{dt^2} \quad (25)$$

where  $\mathbf{K}_T$  is the tangent stiffness matrix,  $\Delta \mathbf{d}$  the displacement increment and  $\mathbf{R}$  the internal force. According to Bathe *et al.* (Bathe *et al.* 1975), Eq. (25) cannot be evaluated directly because of the geometric nonlinearity. It is therefore necessary to iterate Eq. (25) using Newton-Raphson procedure within the time marching scheme.

### 3.4 Newton-Raphson iterations

Applying Newton-Raphson iterations and Newmark- $\beta$  method on the equilibrium iterations per time step, the numerical algorithm for the incremental solution of Eq. (25) are summarized as follows

*Step 1:* Initialize all structural variables

*Step 2:* Calculate Newmark parameters

$$c_0 = \frac{1}{\beta(\Delta t)^2}, \quad c_1 = \frac{\gamma}{\beta\Delta t}, \quad c_2 = \frac{1}{\beta\Delta t}, \quad c_3 = \frac{1}{2\beta} - 1, \quad c_4 = \frac{\gamma}{\beta} - 1,$$

$$c_5 = \left(\frac{\gamma}{2\beta} - 1\right)\Delta t, \quad c_6 = (1 - \gamma)\Delta t, \quad c_7 = \gamma\Delta t$$

*Step 3:* Form the structural mass matrix  $\mathbf{M}$

*Step 4:* Start Newton-Raphson iterations and initialize  $iter = 0$  and  $\Delta\mathbf{d}_{iter} = \mathbf{0}$

*Step 4.1:* Set  $iter \leftarrow iter + 1$

*Step 4.2:* Calculate the tangent stiffness matrix  $\mathbf{K}_T^n$

*Step 4.3:* Evaluate the equivalent stiffness matrix  $\bar{\mathbf{K}}^n = \mathbf{K}_T^n + c_0\mathbf{M}$

*Step 4.4:* Assess the acceleration and displacement of the structure

$$\mathbf{a}_{iter-1}^{n+1} = c_0\Delta\mathbf{d}_{iter-1} - c_2\mathbf{v}^n - c_3\mathbf{a}^n \quad \text{and} \quad \mathbf{d}_{iter-1}^{n+1} = \mathbf{d}^n + \Delta\mathbf{d}_{iter-1}$$

*Step 4.5:* Evaluate the equivalent imbalance load

$$\bar{\mathbf{F}}_{iter-1}^{n+1} = \mathbf{F}^{n+1} - \mathbf{R}_{iter-1}^{n+1} - \mathbf{M}\mathbf{a}_{iter-1}^{n+1}$$

*Step 4.6:* Solve the equation of displacement increment at the  $iter$ th iteration

$$\bar{\mathbf{K}}^n \delta\mathbf{d}_{iter} = \bar{\mathbf{F}}_{iter-1}^{n+1}$$

*Step 4.7:* Obtain the new displacement increment

$$\Delta\mathbf{d}_{iter} = \Delta\mathbf{d}_{iter-1} + \delta\mathbf{d}_{iter}$$

*Step 4.8:* Compute the residuals

$$|\mathbf{g}_{iter}| = |\delta\mathbf{d}_{iter} - \delta\mathbf{d}_{iter-1}|$$

*Step 4.9:* Check convergence and number of iterations

$$\text{If } |\mathbf{g}_{iter}| < tol_{NR} \quad \text{and} \quad iter < iter_{NR,MAX}, \quad \text{then } \Delta\mathbf{d} = \Delta\mathbf{d}_{iter} \quad \text{and go to Step 5}$$

Otherwise, return to *Step 4.1*

*Step 5:* Estimate new acceleration, velocity and displacement of the structure

$$\mathbf{a}^{n+1} = c_0\Delta\mathbf{d} - c_2\mathbf{v}^n - c_3\mathbf{a}^n, \quad \mathbf{v}^{n+1} = \mathbf{v}^n + c_6\mathbf{a}^n + c_7\mathbf{a}^{n+1} \quad \text{and} \quad \mathbf{d}^{n+1} = \mathbf{d}^n + \Delta\mathbf{d}$$

*Step 6:* Proceed to the next time step

The relevant coefficients matrices and vectors have already been provided in (Bathe *et al.* 1975) for the above process.

## 4. Mesh updating technique

### 4.1 Moving submesh approach (MSA)

The dynamic fluid mesh is updated by means of MSA (Lefrançois 2008) in this study. The

basic idea of MSA relies on putting a layer of sparse submesh over a fine fluid mesh which is then dynamically re-arranged through the specific interpolation formulae. Because of two different layers of meshes used, the elements and nodal points on the MSA submesh are labeled *zones* and *nodes* distinctively, whereas those on the fluid finite element mesh are still identified as *elements* and *points*. When complex rigid structures with curvilinear or segments geometries are encountered, a capsule is used to encapsulate them to respect all corners of their profiles. In order to accurately represent a flexible structure's movement and deformation, it is necessary to employ the same level of MSA submesh as that of the structural surface. A resolution of quasi-elasticity equations is required if a submesh contains interior nodes. To that end, the ortho-semi-torsional spring analogy method (OST-SAM) (Markou *et al.* 2007) is used. The resulting quasi-static equilibrium equations arising from OST-SAM are solved by successive over-relaxation technique (Zeng and Ethier 2005) since the number of interior nodes is very small in general.

The main steps of MSA are outlined as follows

*Step 1:* Extract the information of the fluid mesh and the MSA submesh

*Step 2:* Collect the fluid points falling into each zone

*Step 3:* Calculate the interpolation formulae for each fluid point belonging to a zone

*Step 4:* Begin time loop

*Step 4.1:* Gain the motion of wall nodes from the structural movement

*Step 4.2:* If the submesh owns no interior nodes, then go to *Step 4.3*

Or else, invoke OST-SAM for the motion of interior nodes

*Step 4.3:* Update the submesh

*Step 4.4:* Interpolate the fluid mesh according to the new submesh

*Step 4.5:* Check zones and elements' areas

If any area is zero or negative, then stop

Otherwise, proceed to the next time step

*Step 5:* End time loop

Our numerical experience reveals that the cost of MSA is far less than that of SAM, and MSA can well preserve the quality of the ALE mesh topology without resorting to any smoothing of the nodes' coordinates. We also notice that MSA is a variation of the approach proposed by Liu *et al.* (Liu *et al.* 2006). Both approaches adopt the shape functions of a T3 element as their interpolation formulae, but MSA is much simpler for those users who are not familiar with Delaunay graph tools. MSA has been successfully applied to the vortex-induced vibrations (VIV) of a bluff body in our previous works (He *et al.* 2012, He *et al.* 2014, He 2015a,b).

#### 4.2 Geometric conservation law (GCL)

GCL is inevitably encountered in the moving boundary problems. As pointed out in (Lesoinne and Farhat 1996), GCL will be automatically satisfied for the 2D stabilized FEM if the mesh velocity is calculated by

$$\mathbf{w}^{n+1/2} = \frac{\mathbf{x}^{n+1} - \mathbf{x}^n}{\Delta t} \quad (26)$$

Although the midpoint rule (26) is only first-order accurate, it is in wide use and is more suitable than a higher-order scheme in certain case (Förster *et al.* 2007). Despite that, the midpoint rule may break up the velocity continuity on the interface (Farhat and Lesoinne 2000).

It is not trivial to structure the differencing scheme of the mesh velocity for a fractional-step-type fluid solver to fulfill GCL. To this end, a mass source term (MST) (Jan and Sheu 2004) is adopted in this study. Eq. (9) is therefore recast as

$$\nabla^2 p^{n+1} = \frac{1}{\Delta t} \nabla \cdot \tilde{\mathbf{u}} + S_{\text{MST}}^{n+1} \quad (27)$$

with

$$S_{\text{MST}}^{n+1} = \frac{1}{2A_e^{n+1}} \left( \begin{array}{cc} w_1^2 - w_1^1 & w_2^2 - w_2^1 \\ w_1^3 - w_1^1 & w_2^3 - w_2^1 \end{array} \right)^{n+1} \quad (28)$$

where  $A_e^{n+1}$  is the area of element  $e$  at time  $n + 1$ , superscript  $i$  ( $i = 1, 2$  and  $3$ ) in mesh velocity means point  $i$  of element  $e$  and subscript  $j$  ( $j = 1$  and  $2$ ) component  $j$  of coordinates. It should be emphasized that MST is rigorously derived from the T3 element context and it vanishes when a fluid flows on the Eulerian mesh.

## 5. Equilibrium conditions

For partitioned solution approaches, the interplay between a fluid and a structure is achieved by enforcing equilibrium conditions on the interface  $\Sigma$ , amounting to

$$\mathbf{u} = \mathbf{v} \quad \text{on } \Sigma \times [0, T] \quad (29)$$

$$\boldsymbol{\sigma}^{\text{F}} = \boldsymbol{\sigma}^{\text{S}} \quad \text{on } \Sigma \times [0, T] \quad (30)$$

where  $\boldsymbol{\sigma}^{\text{F}} = -\boldsymbol{\tau}^{\text{F}} \cdot \mathbf{n}^{\text{F}}$  and  $\boldsymbol{\sigma}^{\text{S}} = \boldsymbol{\tau}^{\text{S}} \cdot \mathbf{n}^{\text{S}}$  are the fluid and structural tractions respectively,  $\mathbf{n}^{\text{F}}$  represents the unit outward normal of the wet interface and  $\mathbf{n}^{\text{S}} = -\mathbf{n}^{\text{F}}$  means the unit outward normal of the dry interface. Also, the following geometric continuity should be satisfied for the mesh motion

$$\mathbf{x} = \mathbf{d} \quad \text{on } \Sigma \times [0, T] \quad (31)$$

$$\mathbf{w} = \mathbf{v} \quad \text{on } \Sigma \times [0, T] \quad (32)$$

## 6. Partitioned coupling strategies

In the present paper the partitioned coupling strategies consist of the explicit, implicit and semi-implicit schemes based on the previous chapters. A detailed description of each scheme is provided in this section, allowing for a flexible choice to solve FSI problems. Nevertheless, all schemes are used to solve the numerical examples for comparison. Under the consideration of an elastic solid, the matching finite element discretizations have been generated at both sides of the fluid-structural interface in order to avoid the loss of the computational accuracy.

### 6.1 Explicit scheme

The explicit scheme is straightforward to be implemented. The staggered solution of each physical field is advanced in time without the imperative satisfaction of the interfacial conservation. A second-order structural predictor (Piperno 1997) is employed herein. The overall coupling procedure of the explicit scheme is well written as follows

*Step 1:* Initialize all variables

*Step 2:* Extrapolate the position of the interface  $\Sigma$  (Piperno 1997)

$$\tilde{\mathbf{x}}_{\Sigma}^{n+1} = \mathbf{d}_{\Sigma}^n + \left( \frac{3}{2} \mathbf{v}_{\Sigma}^n - \frac{1}{2} \mathbf{v}_{\Sigma}^{n-1} \right) \Delta t$$

*Step 3:* Rearrange the fluid mesh by using MSA

*Step 4:* Calculate the mesh velocity

$$\mathbf{w}^{n+1} = \frac{\tilde{\mathbf{x}}^{n+1} - \mathbf{x}^n}{\Delta t}$$

*Step 5:* Derive the relevant geometric quantities

*Step 6:* Obtain MST for satisfying GCL

$$S_{\text{MST}}^{n+1} = \left( \frac{1}{2A_e} \begin{vmatrix} w_1^2 - w_1^1 & w_2^2 - w_2^1 \\ w_1^3 - w_1^1 & w_2^3 - w_2^1 \end{vmatrix} \right)^{n+1}$$

*Step 7:* Compute the intermediate velocity

$$\tilde{\mathbf{u}} - \mathbf{u}^n = \Delta t \left( -\mathbf{c}^n \cdot \nabla \mathbf{u}^n + \frac{1}{Re} \nabla^2 \mathbf{u}^n + \frac{\Delta t}{2} \mathbf{c}^n \cdot \nabla (\mathbf{c}^n \cdot \nabla \mathbf{u}^n) \right)$$

*Step 8:* Update the fluid pressure

$$\nabla^2 p^{n+1} = \frac{1}{\Delta t} \nabla \cdot \tilde{\mathbf{u}} + S_{\text{MST}}^{n+1}$$

*Step 9:* Correct the fluid velocity

$$\mathbf{u}^{n+1} - \tilde{\mathbf{u}} = -\Delta t \left( \nabla p^{n+1} - \frac{\Delta t}{2} \mathbf{c}^n \cdot \nabla^2 p^n \right)$$

*Step 10:* Deduce the fluid load  $\boldsymbol{\sigma}^{\text{F},n+1}(\mathbf{u}^{n+1}, p^{n+1})$

*Step 11:* Solve the structural equation

$$\mathbf{M}\mathbf{a}^{n+1} + \mathbf{C}\mathbf{v}^{n+1} + \mathbf{K}\mathbf{d}^{n+1} = \mathbf{F}(\boldsymbol{\sigma}^{\text{S},n+1})$$

*Step 12:* Proceed to the next time step

### 6.2 Implicit scheme

It is imperative to require that the equilibrium conditions on the interface should be exactly satisfied at every subiteration per time step for the implicit coupling of the interacting fields when advancing the FSI solution in time. The present implicit scheme employs fixed-point algorithm with Aitken's  $\Delta^2$  accelerator (Küttler and Wall 2008). This technique is of simple operability with good convergence. The main steps of the implicit scheme are described below

*Step 1:* Initialize all variables and  $iter = 0$

Step 2: Extrapolate the position of the interface  $\Sigma$  (Piperno 1997)

$$\tilde{\mathbf{x}}_{\Sigma,iter}^{n+1} = \mathbf{d}_{\Sigma}^n + \left( \frac{3}{2} \mathbf{v}_{\Sigma}^n - \frac{1}{2} \mathbf{v}_{\Sigma}^{n-1} \right) \Delta t$$

Step 3: Start fixed-point iterations

Step 3.1: Set  $iter \leftarrow iter + 1$

Step 3.2: Rearrange the fluid mesh by using MSA

Step 3.3: Calculate the mesh velocity

$$\mathbf{w}_{iter}^{n+1} = \frac{\tilde{\mathbf{x}}_{iter}^{n+1} - \mathbf{x}^n}{\Delta t}$$

Step 3.4: Derive the relevant geometric quantities

Step 3.5: Obtain MST for satisfying GCL

$$S_{MST,iter}^{n+1} = \left( \frac{1}{2A_e} \begin{vmatrix} w_1^2 - w_1^1 & w_2^2 - w_2^1 \\ w_1^3 - w_1^1 & w_2^3 - w_2^1 \end{vmatrix} \right)_{iter}^{n+1}$$

Step 3.6: Compute the intermediate velocity

$$\tilde{\mathbf{u}}_{iter} - \mathbf{u}^n = \Delta t \left( -\mathbf{c}^n \cdot \nabla \mathbf{u}^n + \frac{1}{Re} \nabla^2 \mathbf{u}^n + \frac{\Delta t}{2} \mathbf{c}^n \cdot \nabla (\mathbf{c}^n \cdot \nabla \mathbf{u}^n) \right)$$

Step 3.7: Update the fluid pressure

$$\nabla^2 p_{iter}^{n+1} = \frac{1}{\Delta t} \nabla \cdot \tilde{\mathbf{u}}_{iter} + S_{MST,iter}^{n+1}$$

Step 3.8: Correct the fluid velocity

$$\mathbf{u}_{iter}^{n+1} - \tilde{\mathbf{u}}_{iter} = -\Delta t \left( \nabla p_{iter}^{n+1} - \frac{\Delta t}{2} \mathbf{c}^n \cdot \nabla^2 p^n \right)$$

Step 3.9: Deduce the fluid load  $\boldsymbol{\sigma}_{iter}^{F,n+1}(\mathbf{u}_{iter}^{n+1}, p_{iter}^{n+1})$

Step 3.10: Solve the structural equation

$$\mathbf{M} \mathbf{a}_{iter}^{n+1} + \mathbf{C} \mathbf{v}_{iter}^{n+1} + \mathbf{K} \mathbf{d}_{iter}^{n+1} = \mathbf{F}(\boldsymbol{\sigma}_{iter}^{S,n+1})$$

Step 3.11: Estimate the interfacial residuals

$$\mathbf{g}_{iter} = \mathbf{x}_{\Sigma,iter}^{n+1} - \tilde{\mathbf{x}}_{\Sigma,iter-1}^{n+1}$$

Step 3.12: Check convergence and number of iterations

If  $|\mathbf{g}_{iter}| < tol_{FP}$  and  $iter < iter_{FP,MAX}$ , then proceed to the next time step

Otherwise, go to Step 3.13

Step 3.13: Assess Aitken factor  $\omega_{iter}$  (Küttler and Wall 2008)

Step 3.14: Relax the interface's position

$$\tilde{\mathbf{x}}_{\Sigma,iter}^{n+1} = \omega_{iter} \mathbf{x}_{\Sigma,iter}^{n+1} + (1 - \omega_{iter}) \tilde{\mathbf{x}}_{\Sigma,iter-1}^{n+1}$$

Step 3.15: Go back to Step 3.1

### 6.3 Semi-implicit scheme

In this subsection the semi-implicit scheme is inspired by the projection-based semi-implicit

coupling method (Fernández *et al.* 2007), and thus is called a CBS-based partitioned semi-implicit coupling scheme. The semi-implicit scheme adopts an explicit coupling stage and an implicit coupling stage since the CBS scheme follows the well-known Chorin-Témam splitting (Chorin 1968, Témam 1968). In the explicit coupling stage the first step of the CBS scheme is carried out on a predicted fluid mesh, while, supposing the fluid mesh is fixed provisionally, the other two steps are implicitly coupled with the structural dynamics in the implicit coupling stage. Compared to a fully implicit coupling method, this algorithm reduces the computational effort drastically without compromising stability too much. At the same time all merits of the CBS scheme and the projection-based semi-implicit coupling scheme are inherited. Unlike (Fernández *et al.* 2007), the fluid force loading on the structure is always evaluated using the end-of-step fluid velocity rather than the intermediate one. Within the implicit coupling phase the fluid and structural fields are iterated via fixed-point algorithm with Aitken's  $\Delta^2$  method (Küttler and Wall 2008). The procedure of the semi-implicit scheme is elaborated in the following

*Step 1:* Initialize all variables and  $iter = 0$

*Step 2:* Perform the explicit coupling step

*Step 2.1:* Extrapolate the position of the interface  $\Sigma$  (Piperno 1997)

$$\tilde{\mathbf{x}}_{\Sigma,iter}^{n+1} = \mathbf{d}_{\Sigma}^n + \left( \frac{3}{2} \mathbf{v}_{\Sigma}^n - \frac{1}{2} \mathbf{v}_{\Sigma}^{n-1} \right) \Delta t$$

*Step 2.2:* Rearrange the fluid mesh by using MSA

*Step 2.3:* Calculate the mesh velocity

$$\mathbf{w}_{iter}^{n+1} = \frac{\tilde{\mathbf{x}}_{iter}^{n+1} - \mathbf{x}^n}{\Delta t}$$

*Step 2.5:* Obtain MST for satisfying GCL

$$S_{MST,iter}^{n+1} = \left( \frac{1}{2A_e} \begin{vmatrix} w_1^2 - w_1^1 & w_2^2 - w_2^1 \\ w_1^3 - w_1^1 & w_2^3 - w_2^1 \end{vmatrix} \right)^{n+1}$$

*Step 2.6:* Compute the intermediate velocity

$$\tilde{\mathbf{u}} - \mathbf{u}^n = \Delta t \left( -\mathbf{c}^n \cdot \nabla \mathbf{u}^n + \frac{1}{Re} \nabla^2 \mathbf{u}^n + \frac{\Delta t}{2} \mathbf{c}^n \cdot \nabla (\mathbf{c}^n \cdot \nabla \mathbf{u}^n) \right)$$

*Step 3:* Perform the implicit coupling step and start fixed-point iterations

*Step 3.1:* Set  $iter \leftarrow iter + 1$

*Step 3.2:* Update the fluid pressure

$$\nabla^2 p_{iter}^{n+1} = \frac{1}{\Delta t} \nabla \cdot \tilde{\mathbf{u}} + S_{MST,iter}^{n+1}$$

*Step 3.3:* Correct the fluid velocity

$$\mathbf{u}_{iter}^{n+1} - \tilde{\mathbf{u}} = -\Delta t \left( \nabla p_{iter}^{n+1} - \frac{\Delta t}{2} \mathbf{c}^n \cdot \nabla^2 p^n \right)$$

*Step 3.4:* Deduce the fluid load  $\boldsymbol{\sigma}_{iter}^{F,n+1}(\mathbf{u}_{iter}^{n+1}, p_{iter}^{n+1})$

*Step 3.5:* Solve the structural equation

$$\mathbf{M}\mathbf{a}_{iter}^{n+1} + \mathbf{C}\mathbf{v}_{iter}^{n+1} + \mathbf{K}\mathbf{d}_{iter}^{n+1} = \mathbf{F}(\boldsymbol{\sigma}_{iter}^{S,n+1})$$

*Step 3.6:* Estimate the interfacial residuals

$$\mathbf{g}_{iter} = \mathbf{x}_{\Sigma,iter}^{n+1} - \tilde{\mathbf{x}}_{\Sigma,iter-1}^{n+1}$$

*Step 3.7:* Check convergence and number of iterations

If  $|\mathbf{g}_{iter}| < tol_{FP}$  and  $iter < iter_{FP,MAX}$ , then proceed to the next time step

Otherwise, go to *Step 3.8*

*Step 3.8:* Assess Aitken factor  $\omega_{iter}$  (Küttler and Wall 2008)

*Step 3.9:* Relax the interface's position

$$\tilde{\mathbf{x}}_{\Sigma,iter}^{n+1} = \omega_{iter} \mathbf{x}_{\Sigma,iter}^{n+1} + (1 - \omega_{iter}) \tilde{\mathbf{x}}_{\Sigma,iter-1}^{n+1}$$

*Step 3.10:* Calculate the new mesh velocity on the interface for the fluid boundary condition

$$\mathbf{w}_{\Sigma,iter}^{n+1} = \frac{\tilde{\mathbf{x}}_{\Sigma,iter}^{n+1} - \mathbf{x}^n}{\Delta t}$$

*Step 3.11:* Renew MST for those elements adjacent to the interface

*Step 3.12:* Go back to *Step 3.1*

## 6.4 Aitken's $\Delta^2$ method

Aitken's  $\Delta^2$  method enjoys popularity to accelerate the FSI simulations. The dynamic factor  $\omega_{iter}^{n+1}$  at *iter*th iteration of time  $n + 1$  is estimated by the following recursion formula (Küttler and Wall 2008)

$$\omega_{iter}^{n+1} = \begin{cases} \max(\omega_{MAX}, \omega^n) & iter = 1 \\ -\omega_{iter-1}^{n+1} \frac{\mathbf{g}_{iter-1}^T (\mathbf{g}_{iter} - \mathbf{g}_{iter-1})}{|\mathbf{g}_{iter} - \mathbf{g}_{iter-1}|^2} & iter \geq 2 \end{cases} \quad (33)$$

where  $\omega_{MAX} = 0.1$  and  $\omega_1^0 = 0.5$ .

## 7. Numerical examples

Before presenting our results, we stress that the effects of the mesh resolution and the time step have been fully considered via intense computer experiments. As a consequence, the right choice has been made on the computational parameters for the following numerical examples.

### 7.1 Flutter of a bridge deck

The objective of this example is to simulate a rigid bridge deck with H-profile. The deck is mounted with a vertical spring and a rotational spring, hence being allowed to oscillate vertically and rotate freely. The computational domain along with the boundary conditions is graphically demonstrated in Fig. 1. The bridge deck is exposed to the uniform flows in the horizontal direction and its dimensionless geometry is displayed in Fig. 1. The no-slip boundary condition is applied on the deck surface. The free-stream velocities are prescribed at the inlet and the pressure-free condition is imposed at the outlet. The free boundary condition is assigned to the lateral boundaries. All initial variables are assumed to be zero. The system parameters are set as the same

as those of (Hübner *et al.* 2001, Dettmer and Perić 2006a): the fluid density  $\rho^F = 1.25$ , the fluid viscosity  $\mu = 0.1$ , the inflow velocity  $U = 10$ , the structural mass  $m_2 = 3000$ , the vertical spring stiffness  $k_2 = 2000$ , the mass moment of inertia  $m_\theta = 25300$  and the rotational spring stiffness  $k_\theta = 40000$ . The structural damping is omitted for encouraging the large displacement. The characteristic scale is chosen as the width of the bridge deck  $D = 12$ , thus the Reynolds number is  $Re = \frac{\rho^F U D}{\mu} = 1500$  in this problem. The resulting mass ratios are  $m_2^* = 16.667$  and  $m_\theta^* = 0.976$ . The natural frequencies are  $f_{2,N} = 0.1299$  and  $f_{\theta,N} = 0.2001$ , resulting in the reduced natural frequencies  $f_{2,R} = 0.1559$  and  $f_{\theta,R} = 0.2401$ .

For the sake of computational efficiency, the entire computational domain is divided into three parts: Eulerian subdomain A1, ALE subdomain A2 and Lagrangian subdomain A3. The size of A2 is  $4D \times 4D$  while A3 is made of two rectangles each of which is  $0.95D \times 0.0875D$ . The points in A1 keep fixed at all time while those in A3 move with the rigid body. In A2 the points are dynamically updated by MSA. In order to pay a lower price, some time-invariant matrices in A1 thus are calculated only once at the beginning of the simulation. In Fig. 2(a) the finite element mesh consists of 6486 T3 elements and 3329 points and the corresponding MSA submesh is demonstrated in Fig. 2(b). Since there is no optimal option, a good MSA topology is intuitively requested to fulfill the following two criterions as possible as it can: (1) it has less number of zones; (2) its mesh has the (biaxial) symmetry. The reason why a coarser submesh is better has been stated in (Lefrançois 2008).

As for other computational constants, we prescribe the time step  $\Delta t = 1.0 \times 10^{-2}$ , Newmark parameters  $\beta = 0.25$  and  $\gamma = 0.5$ , the convergence tolerance  $tol_{FP} = 1.0 \times 10^{-6}$ , and the maximum number of iterations  $iter_{FP,MAX} = 50$ . Another concern is the efficiency of the iterative solution under the given conditions. The present computations for fluid-rigid body interaction at most require 4 iterations per time step, and the maximum number will rise to 8 approximately in fluid-flexible body interaction simulations. Typically 1~2 iterations are sufficient at each time step for both kinds of FSI problems, confirming the report from (Habchi *et al.* 2013) that the maximum number of 3 iterations was required at each time step when a stricter convergence tolerance was employed. Thus the computational cost currently remains at a low level.

The computed results are listed in Table 1, including the amplitude of the vertical displacement  $d_{2,MAX}$ , the vertical oscillation frequency  $f_{2,0}$ , the amplitude of the rotational displacement  $d_{\theta,MAX}$  and the rotational oscillation frequency  $f_{\theta,0}$ . From Table 1, a reasonable agreement is observed between the present paper and (Dettmer and Perić 2006a), establishing the good validation of the proposed coupling schemes. The present maxima of the vertical displacement agree well with that of (Dettmer and Perić 2006a). The peaks of the obtained rotational displacement and the obtained oscillation frequency are a bit larger than that of Dettmer and Perić's (Dettmer and Perić 2006a). In particular, the semi-implicit scheme generates the smallest  $d_{\theta,MAX}$  and  $f_{\theta,0}$  that deviate from (Dettmer and Perić 2006a) by 9.77% and 20.81%. Identical to (Dettmer and Perić 2006a), the vertical oscillation frequency coincides with its rotational counterpart. In summary, the difference among our schemes is tiny. In our previous work (He *et al.* 2014), the maximum angle of rotation of a freely rotating rectangular cylinder is also larger than the existing data.

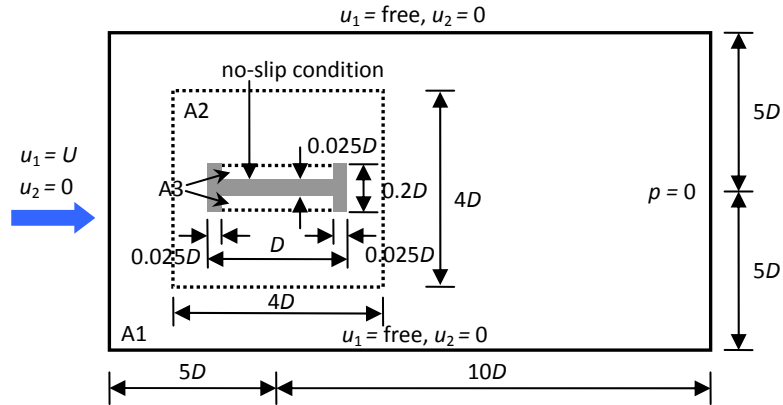
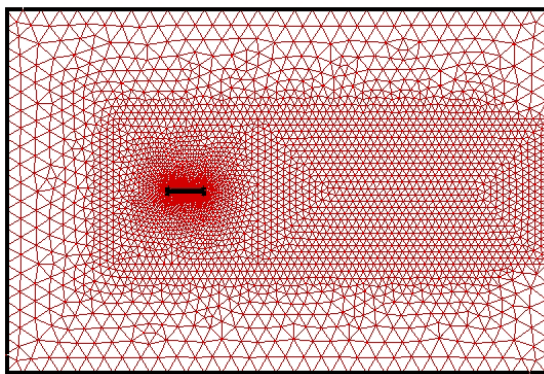
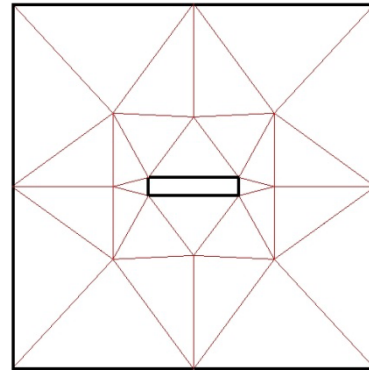


Fig. 1 The geometry and the boundary conditions for an oscillating bridge deck



(a) Finite element mesh for fluid field



(b) MSA submesh for ALE domain

Fig. 2 Mesh and submesh of the problem

Table 1 Comparison of the results for the oscillating bridge deck

Reference	Coupling scheme	$d_{2,MAX}$	$f_{2,0}$	$d_{\theta,MAX}$	$f_{\theta,0}$
Dettmer and Perić (Dettmer and Perić 2006a)	Implicit	0.0625~0.0708	0.186	0.9948	0.186
Present study	Explicit	0.0667	0.2271	1.1455	0.2271
Present study	Implicit	0.0683	0.2271	1.1558	0.2271
Present study	Semi-implicit	0.0656	0.2247	1.0920	0.2247

The time histories of the structural displacements in the vertical and rotational directions are shown in Figs. 3-5. Again, only minor changes are perceived in the time evolution of the structural displacements. The graphs of the vertical displacement are fluctuating. This phenomenon is also implied by Dettmer and Perić (Dettmer and Perić 2006a). In (Dettmer and Perić 2006a) the large-scale vibrations of the bridge deck start at  $t \approx 58$ , and then take a stable pattern at  $t \approx 167$ . The same fact is observed in this paper. Since the rotational oscillation frequency is close to the natural rotational frequency and the vertical oscillation is feeble, the rotation is obviously the dominant motion in this case. The famous flutter phenomenon is clearly seen herein. A typical vorticity field is illustrated in Fig. 6.

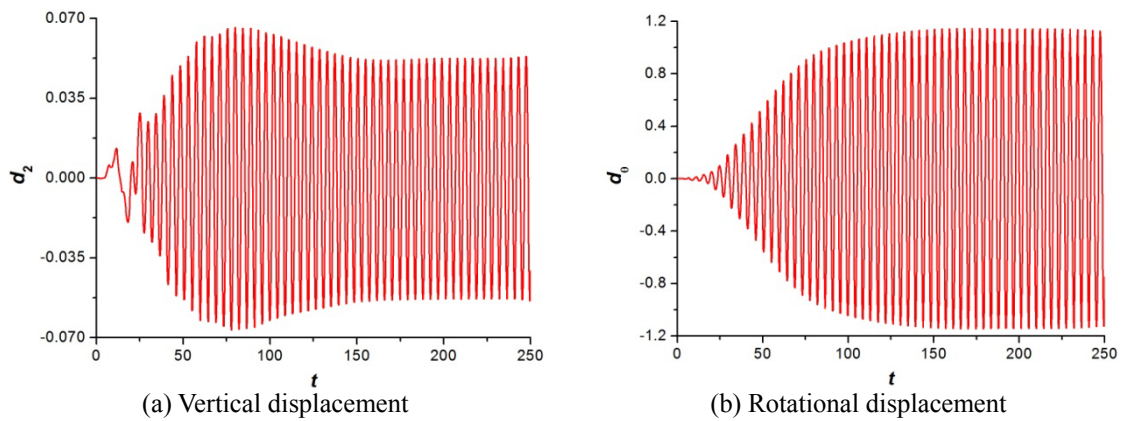


Fig. 3 Time histories of two displacement components using the explicit scheme

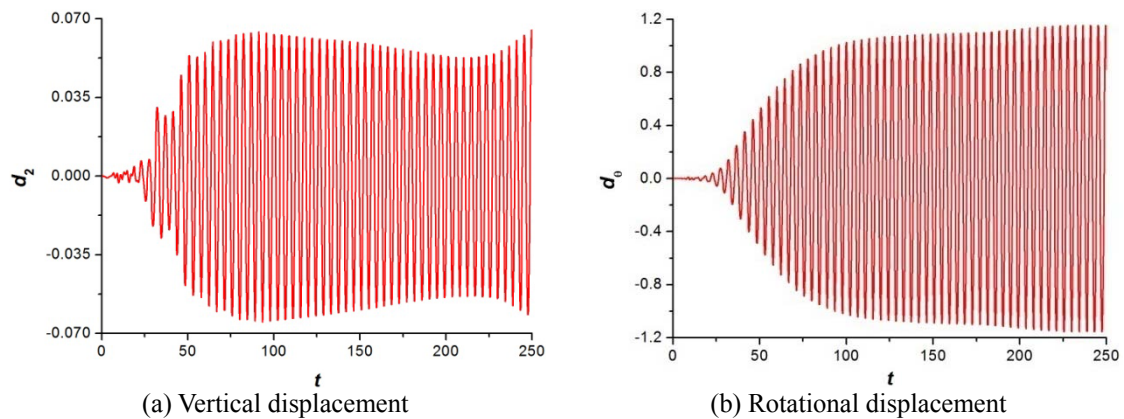


Fig. 4 Time histories of two displacement components using the implicit scheme

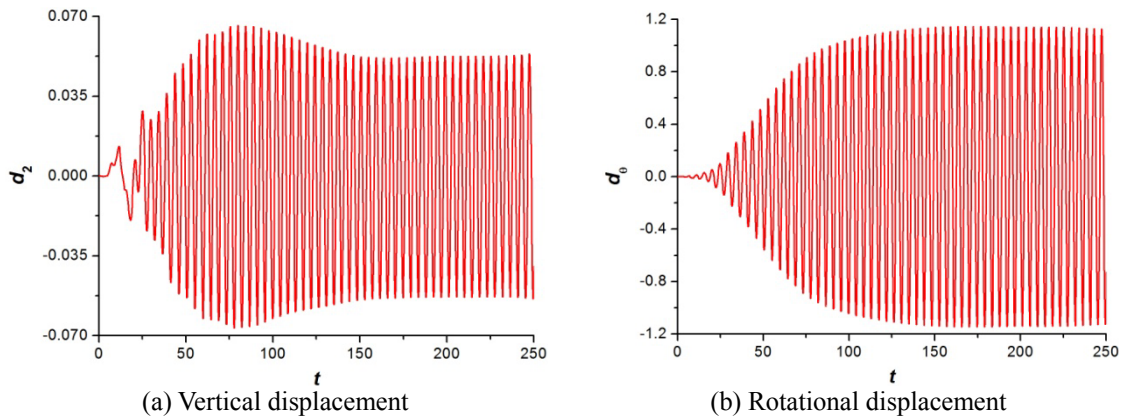


Fig. 5 Time histories of two displacement components using the semi-implicit scheme

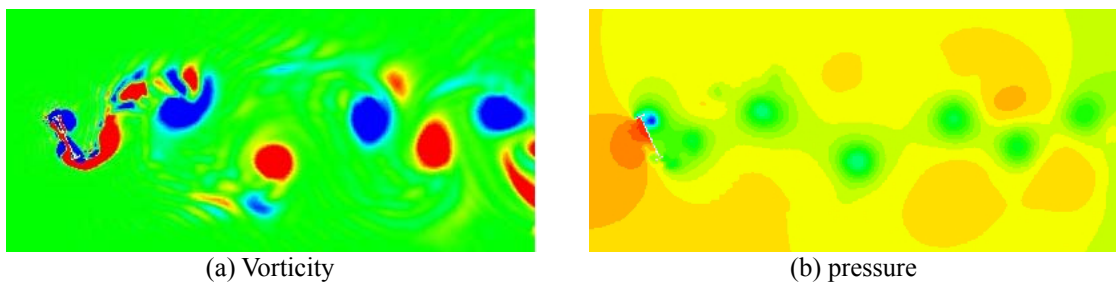


Fig. 6 Instantaneous contours of the bridge deck

### 7.2 VIV of a cantilever attached to a square cylinder

This model problem was originally presented by Wall and Ramm (Wall and Ramm 1998). It is now referred to as a benchmarking problem extensively used to assess the quality of FSI solution algorithms. The geometry and the boundary conditions are plotted in Fig. 7. A fixed square cylinder is submerged in the fluid field, serving as an obstacle with salient edges from which the swirling vortices shed at a certain frequency. A geometrically nonlinear cantilever is attached to the square cylinder in the center of the downstream face, which is excited to oscillate by the time-dependent drag and lift due to the vortex formation in the wake of the obstacle. The no-slip boundary condition is applied on the surfaces of the cylinder and cantilever. The measuring point is placed in the middle of the right edge of the cantilever. The material parameters are as follows (Wall and Ramm 1998): the fluid density  $\rho^F = 1.18 \times 10^{-3}$ , the fluid viscosity  $\mu = 1.82 \times 10^{-4}$ , the structural density  $\rho^S = 1.0 \times 10^{-1}$ , Young's modulus  $E = 2.5 \times 10^6$  and Poisson's ratio  $\nu = 0.35$ . The length scale of the square cylinder is  $D = 1$  and the fluid inflow velocity is  $U = 51.3$ , corresponding to  $Re = 332.6$  in this example.

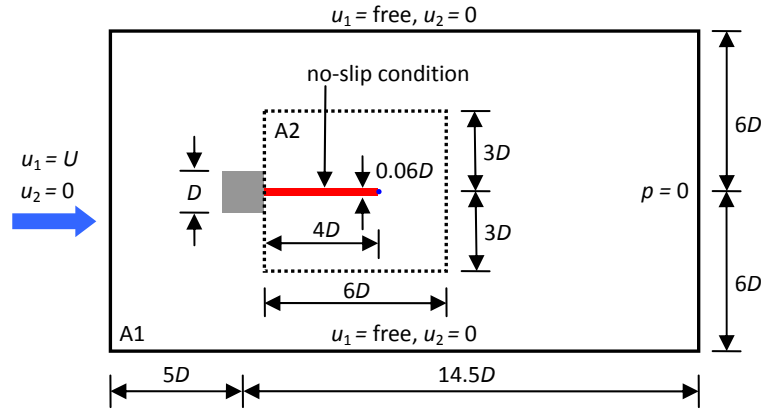
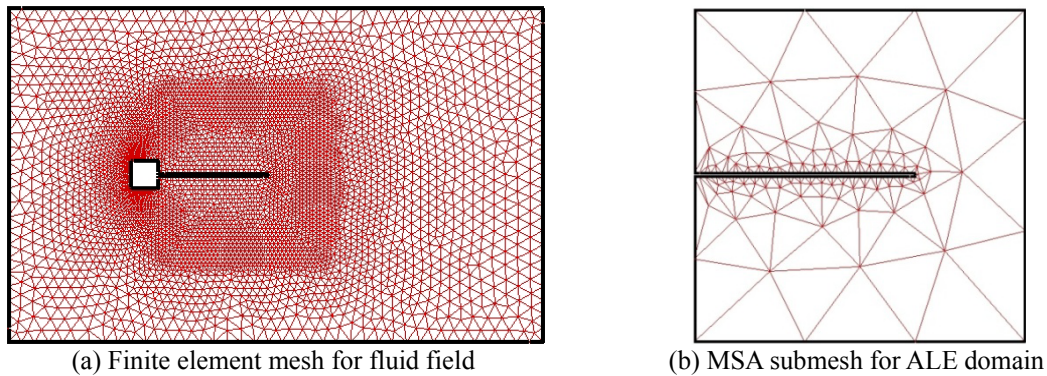


Fig. 7 The geometry and the boundary conditions for a flexible cantilever attached to a square cylinder



(a) Finite element mesh for fluid field

(b) MSA submesh for ALE domain

Fig. 8 Mesh and submesh for the problem

The fluid field is decomposed into Eulerian subdomain A1 and ALE subdomain A2 to reduce the time consumption. A2 is a square box of size  $6D \times 6D$ . The information on grid meshing is assigned as follows. The fluid mesh comprises 8789 T3 elements and 4508 points while the MSA submesh 245 T3 elements and 171 points. The cantilever is discretized with 20 Q9 plane stress elements. The fluid mesh and the MSA submesh are exhibited in Fig. 8. The time step  $\Delta t = 1.0 \times 10^{-2}$  is adopted. The convergence tolerance is  $tol_{FP} = 1.0 \times 10^{-6}$  and the threshold for the number of iterations  $iter_{FP,MAX} = 50$ .  $\beta = 0.5$  and  $\gamma = 0.8$  are chosen for Newmark- $\beta$  method.

Table 2 compares the time-averaged deflection  $\bar{d}_2$  and the time-averaged oscillation frequency  $\bar{f}_0$  of the measuring point with those documented in the open literature (Wall and Ramm 1998, Hübner *et al.* 2001, Matthies and Steindorf 2003, Teixeira and Awruch 2005, Dettmer and Perić 2006b, Liew *et al.* 2007, Bazilevs *et al.* 2008, Wood *et al.* 2008, Yamada and Yoshimura 2008, Braun and Awruch 2009, Olivier *et al.* 2009, Habchi *et al.* 2013). Both quantities are nondimensionalized by  $D$  and  $U$ . It is seen from Table 2 that some difference exists amongst the

published data and a reasonable agreement is observed between the present and existing results. Whilst our schemes give birth to the nearly identical data. The computed mean oscillation frequencies  $\bar{f}_0 = 0.0587$  and  $\bar{f}_0 = 0.0586$  are close to the first eigenfrequency of the flexible thin cantilever  $f_1^S = 0.0591$ , therefore predominating the structural oscillations.

Fig. 9 plots the smooth and undamped time histories of the tip displacement of the flexible cantilever for all schemes, demonstrating that the strong oscillations of the structure induced by the incompressible fluid. In Fig. 9, all cases correctly generate the unsteady periodic long-term oscillatory movements of the geometrically nonlinear cantilever. In accordance with (Dettmer and Perić 2006b, Yamada and Yoshimura 2008), the violent vibrations of the cantilever commences roughly at the dimensionless time 100, namely the real time 2 seconds. But Liew *et al.* (Liew *et al.* 2007) reported that their unsteady long-periodic response came much later.

According to (Liew *et al.* 2007), the displacement history is partitioned into two stages: lock-in and beating. In the first stage, the structural displacement is amplified gradually because the oscillation frequency of the cantilever gets close to its first eigenfrequency, namely the resonance occurs. In the second stage, the structural response converges to the stable long-term oscillatory motion. During the whole course of the structural vibrations, the vortex shedding induces the occurrence of lock-in and drives the flexible cantilever to oscillate sharply, and then the violent oscillations of the flexible cantilever alter the vortex-shedding mode whose frequency derivates from the structural first eigenfrequency.

Table 2 Comparison of the results for the flexible cantilever

Reference	Dimensionality	Coupling scheme	$\bar{d}_2$	$\bar{f}_0$
Wall and Ramm (1998)	2D	Explicit	1.20	0.0604
Hübner <i>et al.</i> (2001)	2D	Monolithic	1.08	0.0615
Matthies and Steindorf (2003)	2D	Implicit	1.18	0.0610
Teixeira and Awruch (2005)	3D	Explicit	1.35	0.0584
Dettmer and Perić (2006b)	2D	Implicit	1.25	0.0634
Liew <i>et al.</i> (2007)	2D	Monolithic	1.34	0.0609
Yamada and Yoshimura (2008)	2D	Implicit	1.19	0.0624
Wood <i>et al.</i> (2008)	3D	Implicit	1.15	0.0573
Bazilevs <i>et al.</i> (2008)	2D	Monolithic	1.21	0.0591
Braun and Awruch (2009)	3D	Explicit	1.181~1.215	0.0600
Olivier <i>et al.</i> (2009)	2D	Implicit	0.95	0.0618
Habchi <i>et al.</i> (2013)	2D	Implicit	1.02	0.0634
Present study	2D	Explicit	1.32	0.0587
Present study	2D	Implicit	1.35	0.0587
Present study	2D	Semi-implicit	1.34	0.0586

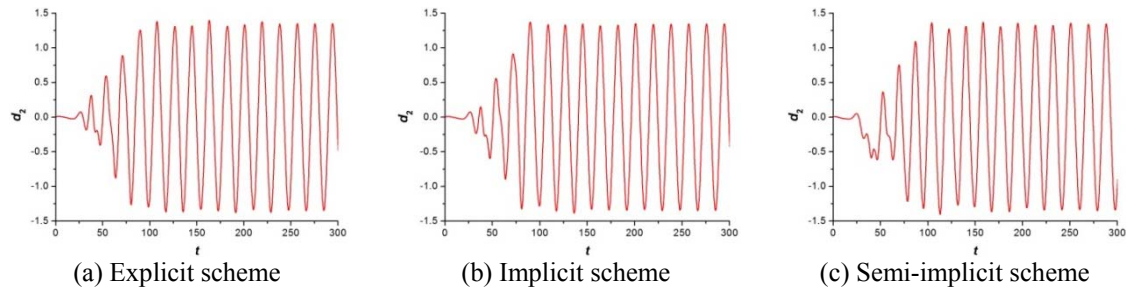


Fig. 9 Time histories of the tip displacement using different schemes

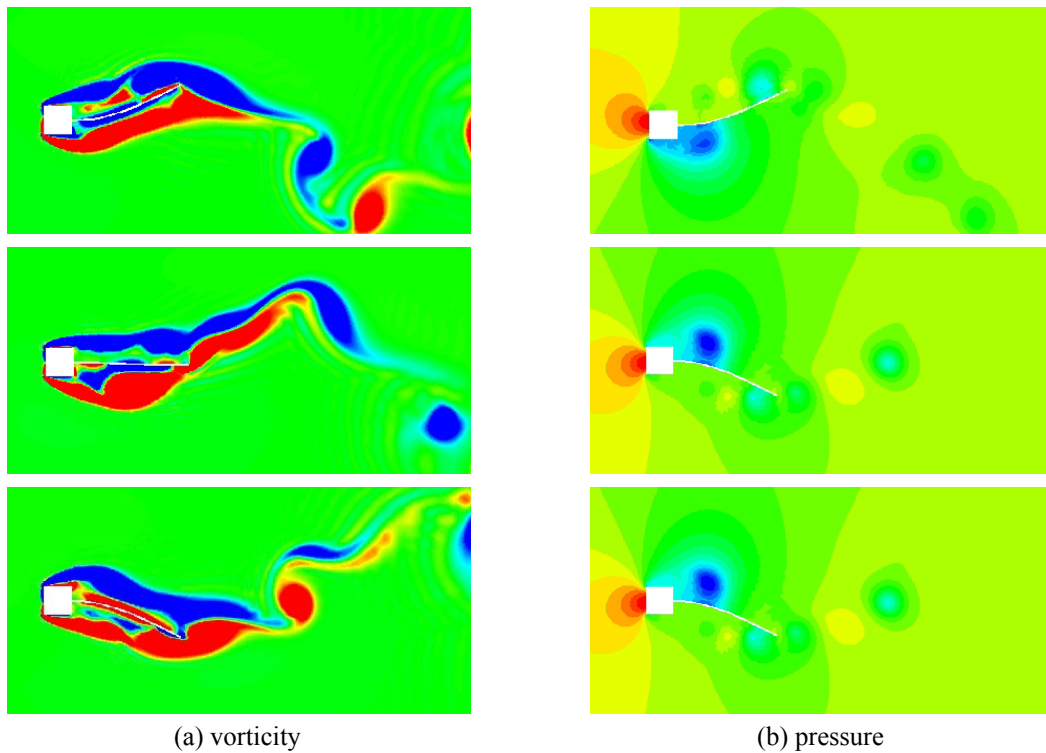


Fig. 10 Instantaneous contours of the flexible cantilever

Fig. 10 displays three typical snapshots of the instantaneous vorticity and pressure fields based on the semi-implicit scheme. The unsteady feature of the flow patterns and the oscillations is distinguished evidently when the oscillations of the cantilever are established totally. In Fig. 10(a) the vortices are alternatively shed from two lateral sides of the square cylinder and then act on the cantilever surface, inducing the strong structural oscillations during an oscillation period. The vortices on one side towards which the flexible cantilever starts to move are weakened and they are eventually suppressed by the flows near the cantilever. High compression is perceived on this side.

However, the vortices on the opposite side are strengthened and advect downstream from the cantilever. These vortices are generated by the velocity gradient at the tip of the cantilever (Habchi *et al.* 2013). Seen from Fig. 10(b), the pressure distribution on the frontal side of the square cylinder is positive due to the immediate exposure of the obstacle to the flows. The high suction (blue zone) can be detected along the lateral sides of the square cylinder. The pressure distribution on the cantilever's surface opposite to the direction of the structural motion is also negative but leads to the lower suction.

In the present study all schemes produce almost the same results although only the results based on the semi-implicit scheme are presented. Interestingly, the comparisons between the explicit and implicit coupling methods for this problem are conflicting (Matthies and Steindorf 2003, Wood *et al.* 2008, Dettmer and Perić 2013).

## 8. Conclusions

This paper has presented three partitioned coupling strategies to deal with the unsteady FSI problems in the ALE finite element framework. The incompressible viscous NS equations are solved by the semi-implicit CBS scheme. A bluff body and an elastic solid are considered as the structural models whose time marching scheme is Newmark- $\beta$  method. In order to take into account the large deformation, the constitutive law of the elastic solid is governed by the Saint Venant-Kirchhoff material. Newton-Raphson procedure is thus utilized to solve the resulting structural nonlinear equations. A hybrid technique, namely MSA in conjunction with OST-SAM, is employed to update the fluid mesh. A mass source term is absorbed by the CBS scheme to easily satisfy geometric conservation law, hence averting the cumbersome construction for the mesh velocity. The proposed coupling algorithms comprise the explicit, implicit and semi-implicit schemes. The first two are fairly easy to be understood in theory and to be implemented in practice, whereas the last one is developed in the similar manner by Fernández *et al.* (Fernández *et al.* 2007). In particular, the semi-implicit scheme contains the explicit and implicit coupling stages thanks to the Chorin-Témam splitting (Chorin 1968, Témam 1968) existing in the CBS scheme. Instructions of all coupling schemes are clearly depicted. Fixed-point algorithm with Aitken's  $\Delta^2$  accelerator is executed for the iterative loops within the implicit and semi-implicit schemes. To validate the proposed schemes, two FSI problems with large structural displacements are considered. The first example is a bridge deck that is excited by the incompressible fluid to oscillate vertically and to rotate in the large angle attitude. Flow-induced vibrations of a flexible cantilever behind a square cylinder are analyzed in the second example. The geometric nonlinearity of the cantilever is fully considered to demonstrate the difficulty of the FSI computation. A good agreement between the present and existing data is observed. All schemes produce the nearly identical results and some well-known flow phenomena are successfully detected.

## Acknowledgments

Supports from Natural Science Foundation of Shanghai (Project No.: 13ZR1430500) are acknowledged.

## References

- Astorino, M., Chouly, F. and Fernández, M. (2009a), “Robin based semi-implicit coupling in fluid-structure interaction: Stability analysis and numerics”, *SIAM J. Sci. Comput.*, **31**(6), 4041-4065.
- Astorino, M., Chouly, F. and Fernández, M.A. (2009b), “An added-mass free semi-implicit coupling scheme for fluid-structure interaction”, *C. R. Acad. Sci. Paris, Ser. I.*, **347**(1-2), 99-104.
- Astorino, M. and Grandmont, C. (2010), “Convergence analysis of a projection semi-implicit coupling scheme for fluid-structure interaction problems”, *Numer. Math.*, **116**(4), 721-767.
- Badia, S., Quaini, A. and Quarteroni, A. (2008), “Splitting methods based on algebraic factorization for fluid-structure interaction”, *SIAM J. Sci. Comput.*, **30**(4), 1778-1805.
- Bathe, K.J., Ramm, E. and Wilson, E.L. (1975), “Finite element formulations for large deformation dynamic analysis”, *Int. J. Numer. Meth. Eng.*, **9**(2), 353-386.
- Bazilevs, Y., Calo, V.M. and Hughes, T.J.R. (2008), “Isogeometric fluid-structure interaction: theory, algorithms, and computations”, *Comput. Mech.*, **43**(1), 3-37.
- Braun, A.L. and Awruch, A.M. (2009), “A partitioned model for fluid-structure interaction problems using hexahedral finite elements with one-point quadrature”, *Int. J. Numer. Meth. Eng.*, **79**(5), 505-549.
- Breuer, M., De Nayer, G. and Münsch, M. (2012), “Fluid-structure interaction using a partitioned semi-implicit predictor-corrector coupling scheme for the application of large-eddy simulation”, *J. Fluid. Struct.*, **29**, 107-130.
- Breuer, M. and Münsch, M. (2008a), “Fluid-structure interaction using LES: A partitioned coupled predictor-corrector scheme”, *Proc. Appl. Math. Mech.*, **8**(1), 10515-10516.
- Breuer, M. and Münsch, M. (2008b), “LES meets FSI: Important numerical and modeling aspects”, *Proceedings of the 7th International ERCOFTAC Workshop on Direct and Large-Eddy Simulation*, Trieste, Italy, September 8-10, 2008.
- Causin, P., Gerbeau, J.F. and Nobile, F. (2005), “Added-mass effect in the design of partitioned algorithms for fluid-structure problems”, *Comput. Method. Appl. M.*, **194**(42-44), 4506-4527.
- Choi, C.K. and Yu, W.J. (2000), “A new ALE finite element techniques for wind-structure interactions”, *Wind Struct.*, **3**(4), 291-302.
- Chorin, A.J. (1968), “Numerical solution of the Navier-Stokes equations”, *Math. Comput.*, **22**(104), 745-762.
- Codina, R., Vázquez, M. and Zienkiewicz, O.C. (1998), “A general algorithm for compressible and incompressible flows. Part III: The semi-implicit form”, *Int. J. Numer. Meth. Fl.*, **27**(1-4), 13-32.
- Dettmer, W. and Perić, D. (2006a), “A computational framework for fluid-rigid body interaction: Finite element formulation and applications”, *Comput. Method. Appl. M.*, **195**(13-16), 1633-1666.
- Dettmer, W. and Perić, D. (2006b), “A computational framework for fluid-structure interaction: Finite element formulation and applications”, *Comput. Method. Appl. M.*, **195**(41-43), 5754-5779.
- Dettmer, W.G. and Perić, D. (2013), “A new staggered scheme for fluid-structure interaction”, *Int. J. Numer. Meth. Eng.*, **93**(1), 1-22.
- Eswaran, M., Goyal, P. and Reddy, G.R. (2013), “Fluid-structure interaction analysis of sloshing in an annular-sectored water pool subject to surge motion”, *Ocean Syst. Eng.*, **3**(3), 181-201.
- Farhat, C. and Lesoinne, M. (2000), “Two efficient staggered algorithms for the serial and parallel solution of three-dimensional nonlinear transient aeroelastic problems”, *Comput. Method. Appl. M.*, **182**(3-4), 499-515.
- Fernández, M.A. (2011), “Coupling schemes for incompressible fluid-structure interaction: implicit, semi-implicit and explicit”, *SeMA J.*, **55**, 59-108.
- Fernández, M.A., Gerbeau, J.F. and Grandmont, C. (2007), “A projection semi-implicit scheme for the coupling of an elastic structure with an incompressible fluid”, *Int. J. Numer. Meth. Eng.*, **69**(4), 794-821.
- Förster, C., Wall, W.A. and Ramm, E. (2007), “Artificial added mass instabilities in sequential staggered coupling of nonlinear structures and incompressible viscous flows”, *Comput. Method. Appl. M.*, **196**(7), 1278-1293.

- Habchi, C., Russeil, S. and Bougeard, D. (2013), "Partitioned solver for strongly coupled fluid-structure interaction", *Comput. Fluids*, **71**, 306-319.
- He, T. (2015a), "On a partitioned strong coupling algorithm for modeling fluid-structure interaction", *Int. J. Appl. Mech.*, Accepted.
- He, T. (2015b), "A partitioned implicit coupling strategy for incompressible flow past an oscillating cylinder", *Int. J. Comput. Methods.*, **12**(3), 1550012.
- He, T., Zhou, D. and Bao, Y. (2012), "Combined interface boundary condition method for fluid-rigid body interaction", *Comput. Method. Appl. M.*, **223-224**, 81-102.
- He, T., Zhou, D. and Han, Z. (2014), "Partitioned subiterative coupling schemes for aeroelasticity using combined interface boundary condition method", *Int. J. Comput. Fluid D.*, **28**(6-10), 272-300.
- Hübner, B., Walhorn, E. and Dinkler, D. (2001), *Strongly coupled analysis of fluid-structure interaction using space-time finite elements*, Cracow, Poland.
- Jan, Y.J. and Sheu, T.W.H. (2004), "Finite element analysis of vortex shedding oscillations from cylinders in the straight channel", *Comput. Mech.*, **3** (2), 81-94.
- Keivani, A. and Shooshtari, A. (2013), "A closed-form solution for a fluid-structure system: shear beam-compressible fluid", *Coupled Syst. Mech.*, **2**(2), 127-146.
- Keivani, A., Shooshtari, A. and Sani, A.A. (2014), "Forced vibration analysis of a dam-reservoir interaction problem in frequency domain", *Coupled Syst. Mech.*, **3**(4), 385-403.
- Küttler, U. and Wall, W. (2008), "Fixed-point fluid-structure interaction solvers with dynamic relaxation", *Comput. Mech.*, **43** (1), 61-72.
- Lefrançois, E. (2008), "A simple mesh deformation technique for fluid-structure interaction based on a submesh approach", *Int. J. Numer. Meth. Eng.*, **75**(9), 1085-1101.
- Lesoinne, M. and Farhat, C. (1996), "Geometric conservation laws for flow problems with moving boundaries and deformable meshes, and their impact on aeroelastic computations", *Comput. Method. Appl. M.*, **134**(1-2), 71-90.
- Liew, K.M., Wang, W.Q. and Zhang, L.X. (2007), "A computational approach for predicting the hydroelasticity of flexible structures based on the pressure Poisson equation", *Int. J. Numer. Meth. Eng.*, **72**(13), 1560-1583.
- Liu, X.Q., Qin, N. and Xia, H. (2006), "Fast dynamic grid deformation based on Delaunay graph mapping", *J. Comput. Phys.*, **211**(2), 405-423.
- Markou, G.A., Mouroutis, Z.S. and Charmpis, D.C. (2007), "The ortho-semi-torsional (OST) spring analogy method for 3D mesh moving boundary problems", *Comput. Method. Appl. M.*, **196**(4-6), 747-765.
- Matthies, H.G. and Steindorf, J. (2003), "Partitioned strong coupling algorithms for fluid-structure interaction", *Comput. Struct.*, **81**(8-11), 805-812.
- Morgenthal, G. and McRobie, A. (2002), "A comparative study of numerical methods for fluid structure interaction analysis in long-span bridge design", *Wind Struct.*, **5**(2), 101-114.
- Murea, C.M. (2007), "A semi-implicit algorithm based on the augmented Lagrangian method for fluid-structure interaction", *Proceedings of the ENUMATH 2007, the 7th European Conference on Numerical Mathematics and Advanced Applications*, Graz, Austria, September 10-14, 2007.
- Murea, C.M. and Sy, S. (2009), "A fast method for solving fluid-structure interaction problems numerically", *Int. J. Numer. Meth. Fl.*, **60**(10), 1149-1172.
- Nagashima, T. and Tsukuda, T. (2013), "Seismic response analysis of an oil storage tank using Lagrangian fluid elements", *Coupled Syst. Mech.*, **2**(4), 389-410.
- Newmark, N.M. (1959), "A method of computation for structural dynamics", *J. Eng. Mech. - ASCE.*, **85**(3), 67-94.
- Nomura, T. and Hughes, T.J.R. (1992), "An arbitrary Lagrangian-Eulerian finite element method for interaction of fluid and a rigid body", *Comput. Method. Appl. M.*, **95**(1), 115-138.
- Olivier, M., Dumas, G. and Morissette, J.F. (2009), "A fluid-structure interaction solver for nano-air-vehicle flapping wings", *Proceedings of the 19th AIAA Computational Fluid Dynamics*, San Antonio, USA, June 22-25, 2009.
- Piperno, S. (1997), "Explicit/implicit fluid/structure staggered procedures with a structural predictor and

- fluid subcycling for 2D inviscid aeroelastic simulations”, *Int. J. Numer. Meth. Fl.*, **25**(10), 1207-1226.
- Quaini, A. and Quarteroni, A. (2007), “A semi-implicit approach for fluid-structure interaction based on an algebraic fractional step method”, *Math. Models Methods Appl. Sci.*, **17**(6), 957-983.
- Sy, S. and Murea, C.M. (2008), “A stable time advancing scheme for solving fluid-structure interaction problem at small structural displacements”, *Comput. Method. Appl. M.*, **198**(2), 210-222.
- Teixeira, P.R.F. and Awruch, A.M. (2005), “Numerical simulation of fluid-structure interaction using the finite element method”, *Comput. Fluids.*, **34**(2), 249-273.
- Témam, R. (1968), “Une méthode d'approximation des solutions des équations Navier-Stokes”, *Bull. Soc. Math. France*, **96**, 115-152.
- Wall, W.A. and Ramm, E. (1998). “Fluid-structure interaction based upon a stabilized (ALE) finite element method”, *Proceedings of the 4th World Congress on Computational Mechanics: New Trends and Applications*, CIMNE, Barcelona, Spain.
- Wood, C., Gil, A.J. and Hassan, O. (2008), “A partitioned coupling approach for dynamic fluid-structure interaction with applications to biological membranes”, *Int. J. Numer. Meth. Fl.*, **57**(5), 555-581.
- Yamada, T. and Yoshimura, S. (2008), “Line search partitioned approach for fluid-structure interaction analysis of flapping wing”, *Comput. Model. Eng. Sci.*, **24**(1), 51-60.
- Zeng, D.H. and Ethier, C.R. (2005), “A semi-torsional spring analogy model for updating unstructured meshes in 3D moving domains”, *Finite Elem. Anal. Des.*, **41**(11-12), 1118-1139.
- Zienkiewicz, O.C. and Codina, R. (1995), “A general algorithm for compressible and incompressible flow. Part I: The split, characteristic-based scheme”, *Int. J. Numer. Meth. Fl.*, **20**(8-9), 869-885.
- Zienkiewicz, O.C., Morgan, K. and Sai, B.V.K.S. (1995), “A general algorithm for compressible and incompressible flow. Part II: Tests on the explicit form”, *Int. J. Numer. Meth. Fl.*, **20**(8-9), 887-913.
- Zienkiewicz, O.C., Nithiarasu, P. and Codina, R. (1999), “The characteristic-based-split procedure: An efficient and accurate algorithm for fluid problems”, *Int. J. Numer. Meth. Fl.*, **31** (1), 359-392.